Journal of the Brazilian Society of Mechanical Sciences and Engineering (2020) 42:493
https://doi.org/10.1007/s40430-020-02572-3

TECHNICAL PAPER

# Multi-fidelity crashworthiness optimization of a bus bumper system under frontal impact

**Erdem Acar[1] · Burak Yilmaz[1] · Mehmet A. Güler[2] · Murat Altin[3]**

Received: 21 May 2020 / Accepted: 13 August 2020 / Published online: 31 August 2020


## Abstract

In this study, crashworthiness of a bus bumper system with a special honeycomb beam is optimized under impact loading using a multi-fidelity optimization approach. The crash performance of the bumper system is evaluated using two metrics: crush force efficiency (CFE) and specific energy absorption (SEA). An optimization with aggregated objectives is performed to seek for an optimum bumper design. Optimum values of the crashbox length, honeycomb wall angle and honeycomb wall thickness are obtained to maximize composite objective function that provides a compromise between these two metrics. Commercial finite element software LS-DYNA is used to compute CFE and SEA values. Multi-fidelity modeling is used to combine data of low-fidelity model at all training points with high-fidelity data at some randomly selected training points to obtain accurate response predictions in less computational time. It is found that multi-fidelity optimization can reduce the computational cost by 33% with only 2% smaller composite objective function value compared to the high-fidelity optimization alternative.

**Keywords** Bumper system · Crashworthiness · Crush force efficiency · Energy absorption · Multi-fidelity optimization

## 1 Introduction

Passenger safety is one of the most essential design elements in automotive industry (in particular, for busses and coaches) and gains more importance day by day. To protect driver and co-driver for a bus or coach in case of a collision, engineers study how to build crashworthy vehicles. Energy-absorbing elements are among the main structures used in vehicle design to achieve this goal. These structures absorb crash energy by transforming it into strain energy, while they deform. Due to huge occurrence ratio of frontal crashes among all, bumper systems are the most important and most studied energy-absorbing structures in vehicle design.

Crashboxes are the main energy-absorbing components of the structure, while the bumper beam has more rigid structure to transmit crash energy to the crashboxes in various crash scenarios with a less energy-absorbing capability. Therefore, substantial number of studies is performed on crashboxes with various shapes, such as cylindrical straight tubes [1–3], square extrusions [4–6] and multi-cell cross-sectioned tubes [7–11]. It is found that these structures are efficient energy absorbers that have capability to crush and fold stably. Many researchers studied on tapered circular tubes [12–14] and tapered rectangular tubes [15–17]. They showed the energy absorption advantages of tapered tubes under axial impact. In many studies honeycomb [18–22] and foam [18, 23–26] filling of these thin-walled tubes are investigated. These studies show that honeycomb structures and aluminum foams are significantly improved the crash performance of crashboxes.

Technical Editor: João Marciano Laredo dos Reis.

✉ Erdem Acar
acar@etu.edu.tr

Burak Yilmaz
burakyilmaz@etu.edu.tr

Mehmet A. Güler
mehmet.guler@aum.edu.kw

Murat Altin
maltin@gazi.edu.tr

1 Department of Mechanical Engineering, TOBB University of Economics and Technology, Ankara, Turkey

2 College of Engineering and Technology, American University of the Middle East, Egaila, Kuwait

3 Department of Automotive Engineering, Gazi University, Ankara, Turkey

There exist many studies on shape design of bumper beams to increase their crash performance [27–34]. These studies show that energy-absorbing capability of a bumper can be improved by using different shapes and optimizing them. Li et al. [35] studied optimization of foam-filled bumper beams and found that foam filling increases the energy absorption capability of a bumper. Jacob and Arunkumar [36] determined that foam and honeycomb incorporated bumpers absorb significantly more energy compared to a hollow steel bumper.

Finite element (FE) simulations are crucial design tools for engineers to design crashworthy vehicles. In order to obtain realistic results, high degrees of fidelity and robust simulations must be performed. However, this ability to design competitive products comes with a cost. The higher the fidelity of the FE model is, the higher the computational cost. A full FE crash simulation of a vehicle takes hours to complete. Also, many simulations must be performed in order to optimize a multi-variable design depending on the number of variables and the expected precision. Combination of these two may induce days of FE analysis and eventually leads to increased design time and cost.

However, there is an optimization concept called multi-fidelity modeling that gains popularity as a remedy for the computational burden [37–44]. This method essentially combines different fidelity FE model results to obtain high accuracy with significantly improved computational time. After creating a low-fidelity model complementary to the high-fidelity model, few high-fidelity analyses are performed at some design points and a function is used to calculate the offset between high-fidelity and low-fidelity results. Then, optimization runs are performed on low-fidelity model and predicted high-fidelity results are calculated using the offset function. This method helps to decrease computational cost by allowing designers to perform all optimization analyses using computationally inexpensive low-fidelity model with few costly high-fidelity simulations instead of running all simulations on high-fidelity FE model. It should be noted that the multi-fidelity approach used in this study is similar to the space mapping approach, which has been used in various applications including crashworthiness optimization [45], friction stir welding [46], fluid–structure interaction [47], airfoil shape optimization [48] and others [49, 50].

In this study, the effects of various geometrical parameters such as length of the crashboxes, wall angle and wall thickness of honeycomb on crash performance of a honeycomb filled bumper are investigated. A commercial finite element (FE) analysis software LS-DYNA [51] is used to simulate crash behavior of the bumper system under impact conditions of ECE R-29 tests [52]. The constructed finite element model is validated by using experimental results available in the literature. The optimum values of geometrical variables are obtained through multi-objective optimization by maximizing a composite objective function that provides a compromised value between crush force efficiency and specific energy absorption.

This paper is structured as follows. The next section provides the problem description for the optimization of honeycomb structure filled bumper system. Section 2 presents the details of finite element model and its validation. Section 4 explains multi-fidelity optimization concept. Section 5 describes construction of surrogate models and their accuracies. Section 6 discusses high-fidelity, low-fidelity and multi-fidelity optimization results. The paper is concluded with some remarks given in Sect. 7.

## 2 The bumper system

Description of the problem of interest, the crash metrics used and the formulation of the optimization problem are explained in the following sub-sections.

### 2.1 Problem description

The original study of this paper stems from the occupant safety systems for busses. The existing safety regulation for frontal impact for trucks is ECE R-29, and it is adapted for safety of driver and co-driver of busses [53]. The pendulum test according to ECE R-29 regulation is shown in Fig. 1. A bumper system having honeycomb structures inside the bumper beam is analyzed in this study. The generic model of the bumper system is shown in Fig. 2.

All designs have the same bumper beam with length of 1112 mm, height of 129 mm, width of 65 mm and wall thickness of 1 mm. Two crashboxes in the model have the following dimensions, height of 120 mm, width of 80 mm, wall thickness of 1.6 mm and length of $L$ (see Fig. 3).

Bumper beam is filled with two pieces of honeycomb structures in front of each crashbox with length of 200 mm, height of 128 mm, width of 64 mm, cell edge length of 20 mm, angle of cell walls $\theta$ and wall thickness of honeycomb $t$ (see Fig. 4).

Examples of four different honeycomb structures with different cell wall angle used in FE models are shown in Fig. 5. In crash performance optimization for the bumper, three dimensions are chosen as design variables: (i) the length of the crashboxes $L$, (ii) the angle of cell walls $\theta$ and (iii) the wall thickness of honeycomb $t$.

For the crash performance evaluation of the bumper system, the following design problem is considered. The bumper system is assembled at the front end of a generic heavy vehicle chassis, while the chassis is attached to a stiff fixture. Then, the whole assembly is placed in front of a rigid

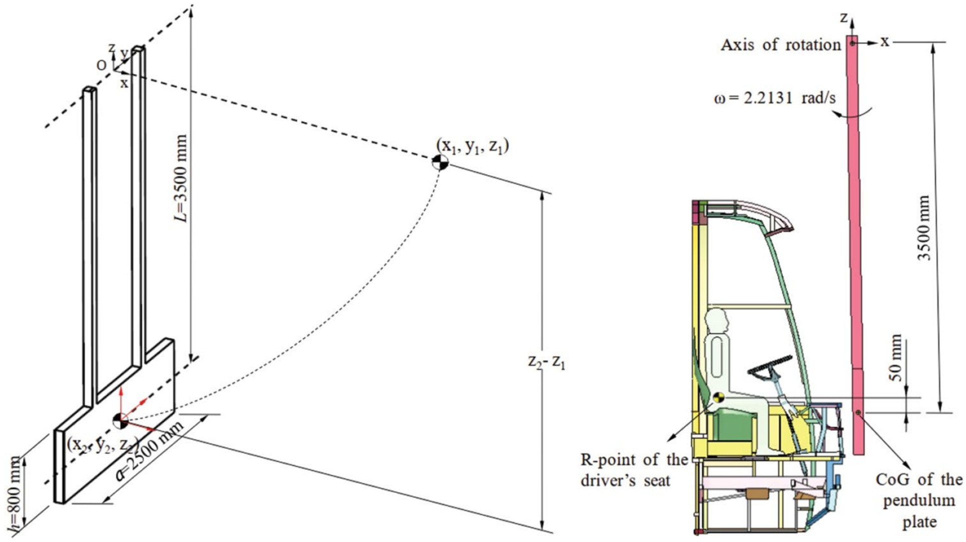


**Fig. 1** Pendulum test according to ECE R-29 regulation

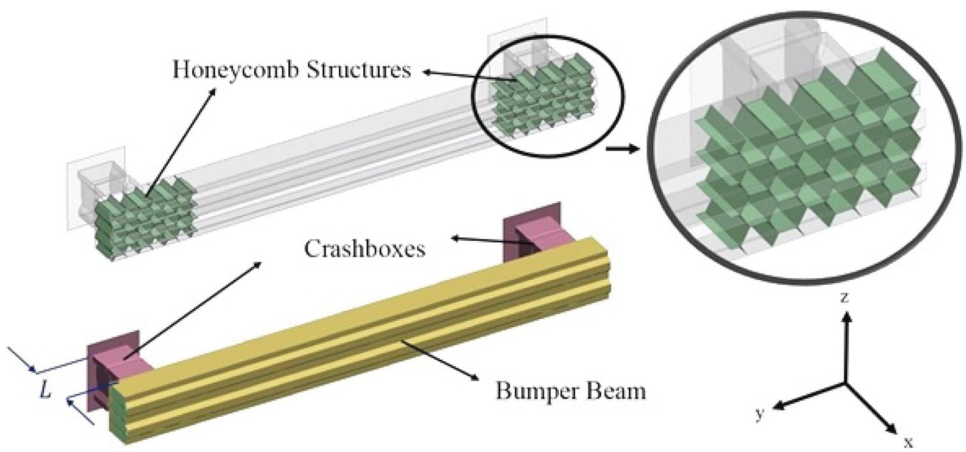


**Fig. 2** Bumper system

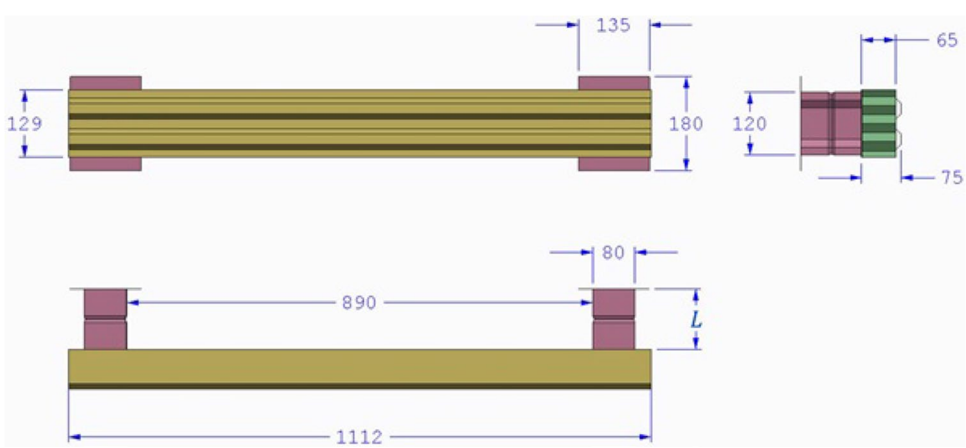


**Fig. 3** Dimensions of the bumper system

pendulum. Bumper system is impacted with the 1500-kg pendulum that has initial kinetic energy of 45 kJ in accordance with United Nations' ECE R-29 safety requirements for heavy commercial vehicles [52].

## 2.2 Crash performance metrics

Total energy ($E_t$) absorbed by the structure is defined as work done by the crushing force $P$ over the deformation distance $d$ (the maximum deformation before elastic rebound).

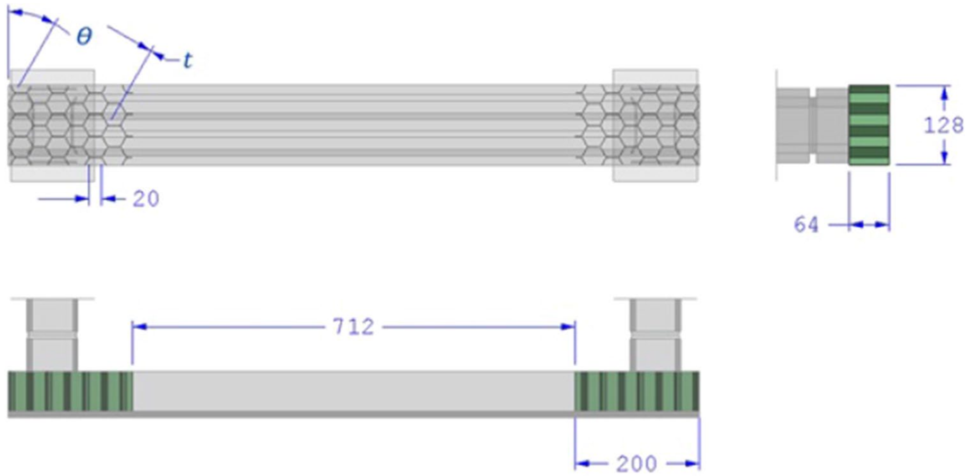


Fig. 4 Dimensions of the honeycomb structures

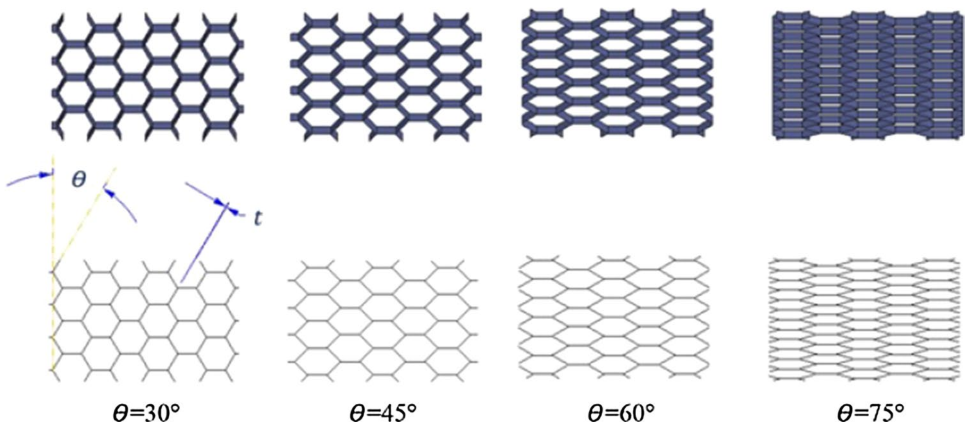


Fig. 5 Honeycomb with various design with different $\theta$

$$E_t = \int_0^d P\,dx \tag{1}$$

Mean crush force (MCF) for a deformation is defined as the total energy absorbed by the structure divided by the deformation distance, $d$ as:

$$\mathrm{MCF} = \frac{E_t}{d} \tag{2}$$

Crush force efficiency (CFE) is defined as the ratio of the mean crush force (MCF) to the peak crush force (PCF) to evaluate the efficiency of an energy absorber.

$$\mathrm{CFE} = \frac{\mathrm{MCF}}{\mathrm{PCF}} \tag{3}$$

where we used SAE-1000 filter in force–displacement curve while determining the PCF.

Specific energy absorption (SEA) is calculated as the total energy absorbed ($E_t$) divided by the mass of the absorber structure ($m$), and it is calculated as:

$$\mathrm{SEA} = \frac{E_t}{m} \tag{4}$$

### 2.3 Formulation of the optimization problem

In this study, crashworthiness of the bumper system is evaluated by using CFE and SEA, so that the bumper system is designed to maximize these two metrics. As noted earlier, three design variables are chosen: (1) length of the crashboxes, $L$, (2) wall angle of honeycomb cells, $\theta$ and (3) wall thickness of honeycomb cells, $t$. Thus, the optimization problem can be stated as:

$$\begin{aligned} &\text{Min} \;\; -f \\ &\text{S.t.} \;\; 80\text{ mm} \le L \le 160\text{ mm} \\ &\qquad 30^\circ \le \theta \le 75^\circ \\ &\qquad 0.25\text{ mm} \le t \le 0.75\text{ mm} \end{aligned} \tag{5}$$

Here $f$ is a composite objective function that can provide a compromise between SEA and CFE. The composite objective function can be defined as:

$$f = w\frac{\mathrm{CFE}}{\mathrm{CFE}_0} + (1-w)\frac{\mathrm{SEA}}{\mathrm{SEA}_0} \quad (6)$$

where $w$ is the weight factor to determine the importance of the metrics relative to each other. For this study weight factor is selected as 0.5 because both metrics are decided to be equally important. $\mathrm{CFE}_0$ and $\mathrm{SEA}_0$ are the normalization constants for CFE and SEA. Normalization constants are taken as maximum values of CFE and SEA at training points (see Sect. 5.2).

The optimization problem defined above is solved by using "ga" built-in function of MATLAB that uses genetic algorithm [54]. The population size is taken as 100, the elite count is taken 6, the crossover fraction is taken 80%, the maximum number of generations is taken 300, and remaining algorithm parameters are taken the default values in MATLAB.

## 3 Finite element modeling

Finite element method is used in this study to calculate crash behavior of the bumper system. In this section finite element (FE) model and validation of the FE model will be explained.

### 3.1 Validation of the FE Model of the Honeycomb Structure

The validation study is based on the experimental study by Zhang et al. [55], where a honeycomb structure is crushed with a rigid wall. The FE model prepared in this study is shown in Fig. 6 next to the experimental model of Zhang et al. [55].

Before the validation runs of the FE model, a mesh convergence study is performed on the base model. Mesh convergence decision is based on the mean crush force value. MCF, CFE and SEA comparison graphs of FE models having 0.5 mm, 1 mm, 1.5 mm, 1.75 mm, 2 mm and 2.5 mm mesh sizes are shown in Fig. 7. It is seen that the MCF, CFE and SEA values settle as mesh size decreases. From Fig. 7, the mesh size is determined as 0.5 mm to be used for all validation runs.

In this study, $3 \times 3$ and $5 \times 5$ honeycomb cell configurations are used for honeycombs as given in Zhang et al. [55]. For both $3 \times 3$ and $5 \times 5$ cell configurations, the height of honeycombs is taken as 100mm, honeycomb wall thickness is taken as 0.075 mm, and the central angle $\alpha$ is taken as 120°. Wall thickness of the honeycombs is doubled where two metal sheets are glued together because of the production method of honeycombs as shown in Fig. 8.

For the contact algorithm, "AUTOMATIC_SINGLE_SURFACE_CONTACT" is defined between the honeycomb and the fixed wall, "AUTOMATIC_SURFACE _TO_SURFACE_CONTACT" between the honeycomb structure and the moving wall as shown in Fig. 6. Static and dynamic friction coefficients are taken as 0.3 and 0.2, respectively. Belytschko–Tsay 4-noded shell element type is used as element type. To simulate AA3003 H18 aluminum foil material in the reference experimental study, "MAT_24_PIECEWISE_LINEAR_PLASTIC" material definition is used. This material model is widely used in crash simulations related to automotive industry [13, 51].

As a result of this validation study, load–displacement graphs for $3 \times 3$ and $5 \times 5$ cell configurations shown in Fig. 9 are obtained. Along with the load–displacement curves, energy absorption values of honeycomb structures are also calculated and compared with the reference experimental results. Note that Figure 7 of Zhang et al. [55] is digitized by using GetData Graph Digitizer, and the corresponding force and displacement values are extracted. Then, the area under force–displacement curve is obtained by using OriginPro graphical software to calculate the energy absorption. Energy absorption of FE analyses and experimental results are tabulated in Table 1. Comparison of experimental and numerical collapsed models with $3 \times 3$ and $5 \times 5$ cell

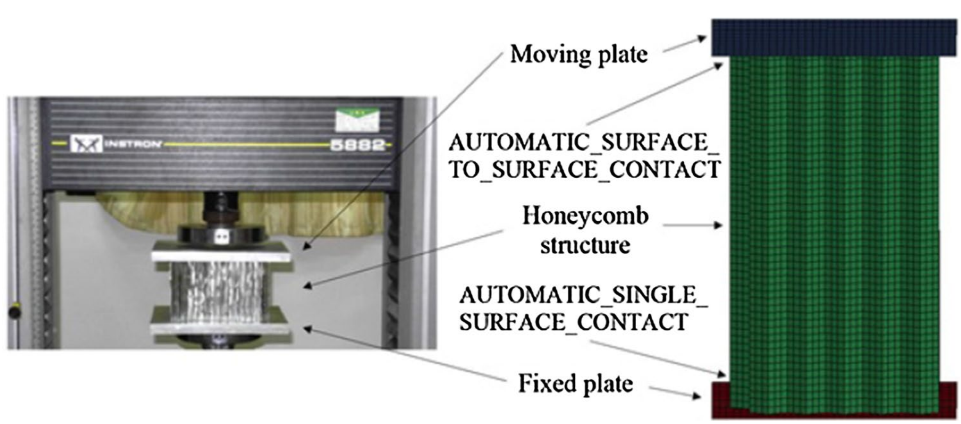


**Fig. 6** Experimental setup of Zhang et al. [55] on the left, and FE validation model on the right

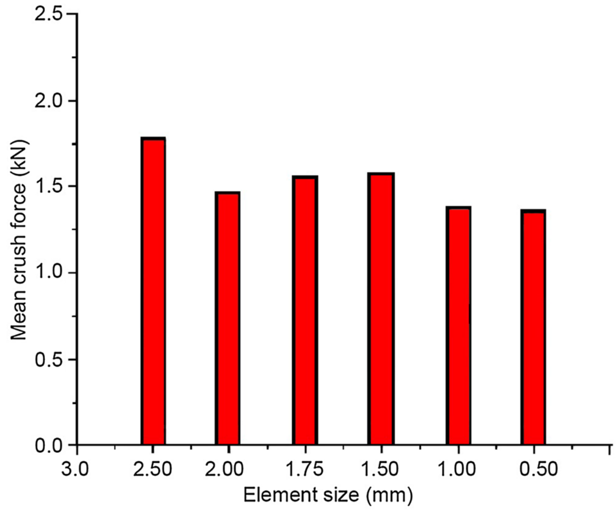

**(a)** Mean crash force comparison

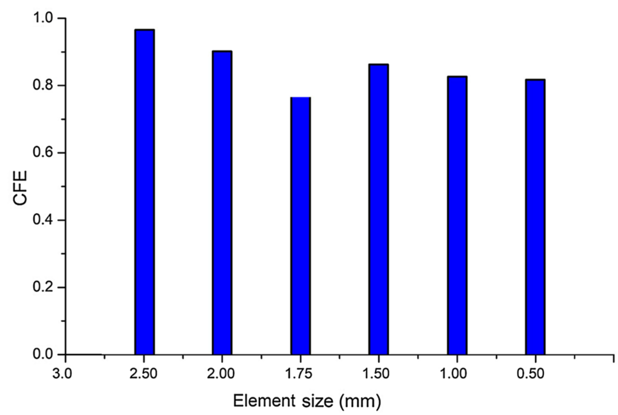

**(b)** CFE comparison

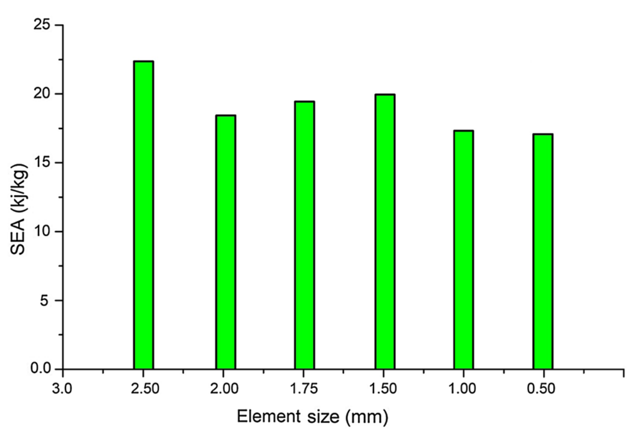

**(c)** SEA comparison

**Fig. 7** Mesh convergence study for the FE model of the honeycomb structure

configurations is shown in Fig. 10. It is seen that the FE results are in good agreement with the experimental results of Zhang et al. [55].

### 3.2 Description of the FE model

The response of bumper systems under impact loading is predicted by using nonlinear, explicit finite element software LS-DYNA [51]. The finite element model is prepared as shown in Fig. 11. Bumper system is attached to a generic heavy vehicle chassis (see Sect. 2.1 for the detailed explanation of the bumper system). For the contact algorithm ”TIED_SURFACE_TO_SURFACE_CONTACT” is defined between endplates of crashboxes and chassis. Then, this assembly is attached to a fixture that is designed to hold the position of attached test sample and withstand crushing force of the pendulum. Again, ”TIED_SURFACE_TO_SURFACE _CONTACT” is defined between endplates of chassis and the front surface of fixture. Next, the whole unit is placed in front of a 1500-kg pendulum modeled according to ECE R-29 test standards [52]. Bottom surfaces of the fixture that touches the ground are fixed to maintain the position of the assembly during impact. All degrees of freedom of nodes that form the axis of pendulum are also fixed except rotation around y-axis, which allows pendulum to rotate (see Fig. 11). ”AUTOMATIC_SINGLE_SURFACE_CONTACT” is defined as containing all surfaces forming bumper system to prevent interference between the surfaces. For the contact algorithm ”AUTOMATIC_SURFACE_TO_SURFACE_CONTACT” is defined between pendulum and bumper system. Static and dynamic friction coefficients are taken as 0.3 and 0.2, respectively. The reader is referred to [56] for the details of the finite element analysis of the pendulum test setup.

Belytschko–Tsay 4-noded shell element type is used to generate elements. Materials of parts are determined as follows: ST44 steel for the fixture, DP1300 steel for the bumper beam, DP600 steel for the crashboxes, DP780 steel for the chassis and AA303 H18 aluminum for the honeycomb structures. To simulate these materials in FE model, ”MAT_24_PIECEWISE_LINEAR_ PLASTIC” material definition is used. ”MAT_20_RIGID” material definition is used for the pendulum.

Crash energy of the pendulum is provided via defining an initial angular velocity and inertia around y-axis. Inertia of the pendulum around y-axis is taken as $I_{yy} = 18.38 \times 10^6$ t×mm$^2$, and angular velocity around y-axis is taken as $\omega = 2.21$ rad/s to provide 45 kJ crash energy. These values are taken from a previous study performed by Guler et al. [56]. Note that the crash energy requirement of 45 kJ was increased to 55 kJ in the latest version of ECE R-29.

Two-step mesh convergence study is performed to determine the mesh sizes of the bumper system components. In the first step, FE models having 3, 4, 5 and 6 mm mesh size for the bumper beam and crashboxes are analyzed. Mean crush force comparison of FE models is shown in Fig. 12. It is seen that the mean crush force value settles as the mesh

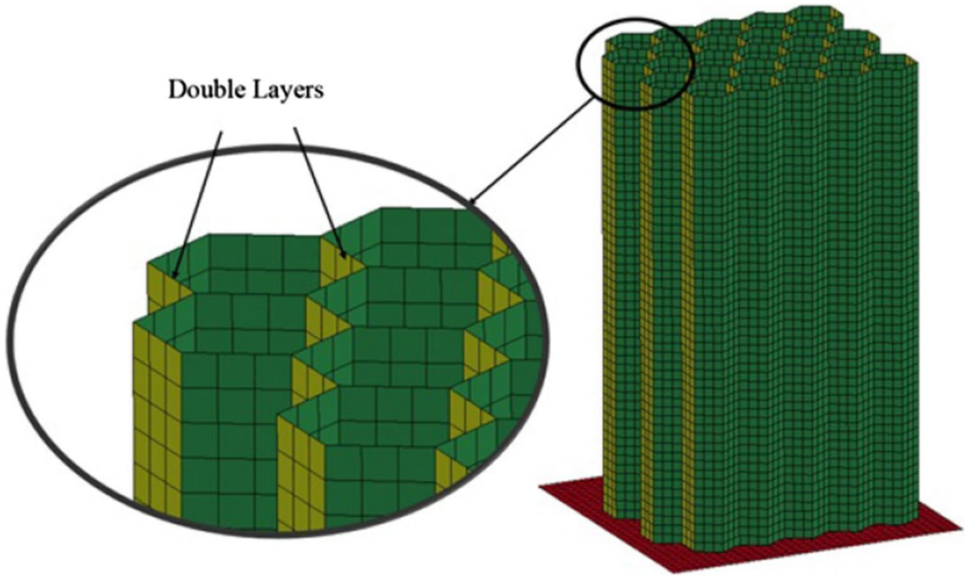


**Fig. 8** Contacts and double-layer surfaces of FE validation model

**Table 1** Energy absorption comparison of FE analyses and experimental results of Zhang et al. [55]

| Cell Configuration | FE results of Validation study | Experimental Results [55] | Error (%) |
|---|---|---|---|
| $3 \times 3$ | 40.11 J | 39.46 J | 1.6 |
| $5 \times 5$ | 104.0 J | 99.12 J | 4.7 |

size decreases. From Fig. 12, the mesh size is determined as 4 mm for bumper beam and crashboxes.

In the second step, FE models having 2.5, 3.0, 3.5, 4.0 and 5.0 mm mesh size for honeycomb structures are analyzed. Mean crush force comparison of FE models is shown in Fig. 13. Using the similar approach as before, the mesh size of honeycomb structures is determined as 3 mm (see Fig. 13).

After determination of bumper beam, crashbox and honeycomb mesh sizes via a second mesh convergence study, the mesh sizes of the remaining parts are selected by intuition as they are subjected to much less deformation than bumper system. As shown in Fig. 14, mesh size of the chassis and the fixture is determined as 4 mm and 10 mm, respectively. Therefore, a base FE model is fully constructed to simulate crash performance of designed bumper system.

As shown in Fig. 15, two different finite element (FE) models with different fidelities are used in this study. Previously constructed FE model is the complete model which consist of bumper system (that includes bumper beam, two crashboxes and two pieces of honeycomb structures),

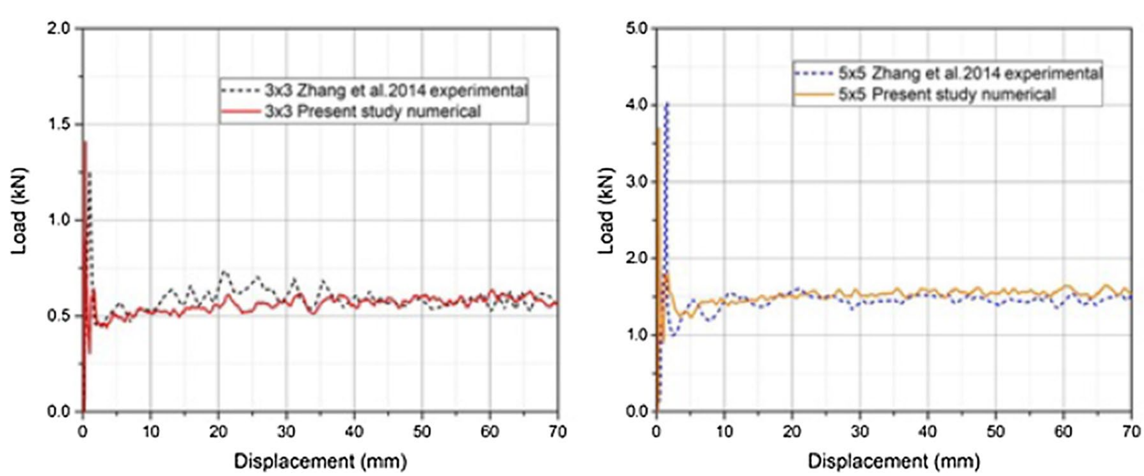


**Fig. 9** $3 \times 3$ cell configuration (on the left), $5 \times 5$ cell configuration (on the right). Load–displacement graph comparisons of FE analyses and experimental results of Zhang et al. [55]

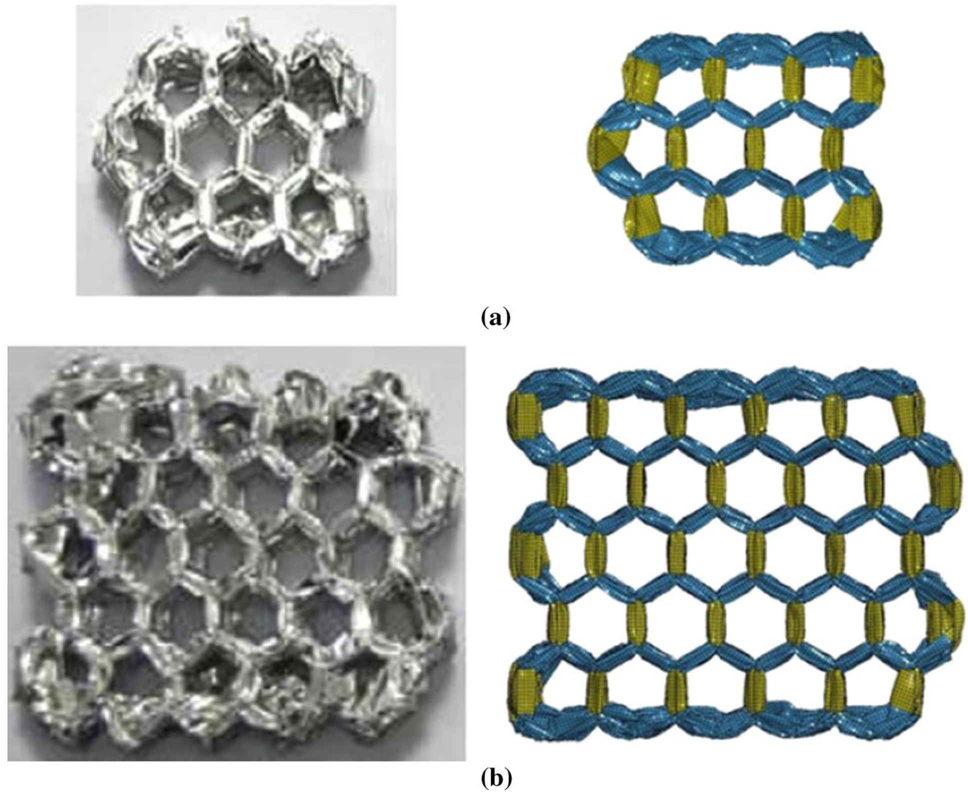


**Fig. 10** Comparison of **a** 3 × 3, and **b** 5 × 5 cell configuration experimental result of Zhang et al. [55] and numerical results

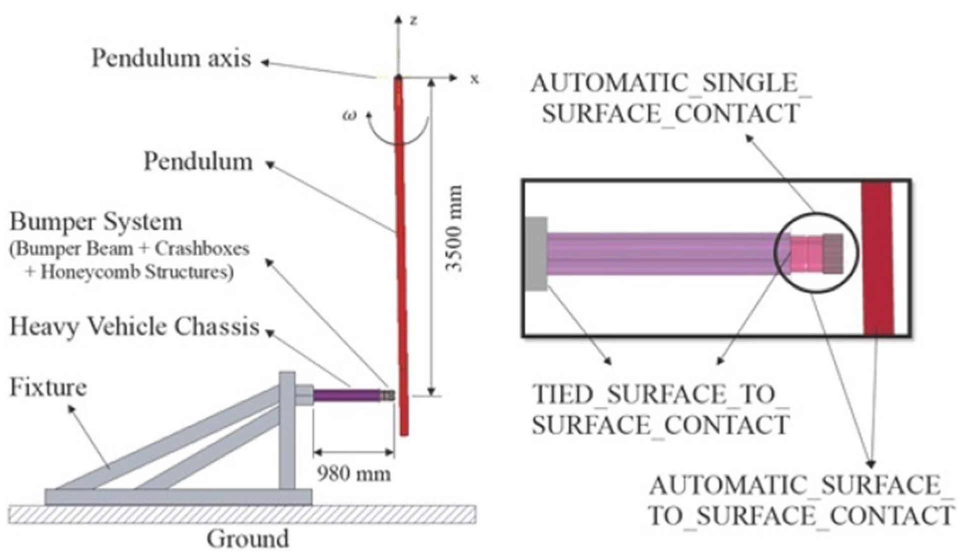


**Fig. 11** Finite element setup

vehicle front rails and fixture that places the structure in front of the rigid pendulum. This complete model is named as high-fidelity (HF) model. The surfaces of fixture that touch to the ground are fixed in this FE model. A low-fidelity FE model is derived from the HF model. Fixture and heavy vehicle chassis are subtracted from the HF model to obtain low-fidelity (LF) model, which consist of only the bumper system. The bumper system is fixed from the end plates of the crashboxes. ”TIED_SURFACE_TO_SURFACE_CONTACT” is deleted as corresponding parts do not exist, while all other FE model definitions remained identical to HF model. The comparison between the LF and HF models based on the force–displacement behavior for the baseline model is shown in Fig. 16. One FE simulation takes approximately 14 h for the HF model and 2.5 h for the LF model, with two Intel Xenon 3.1 GHz processors and 64 GB RAM.

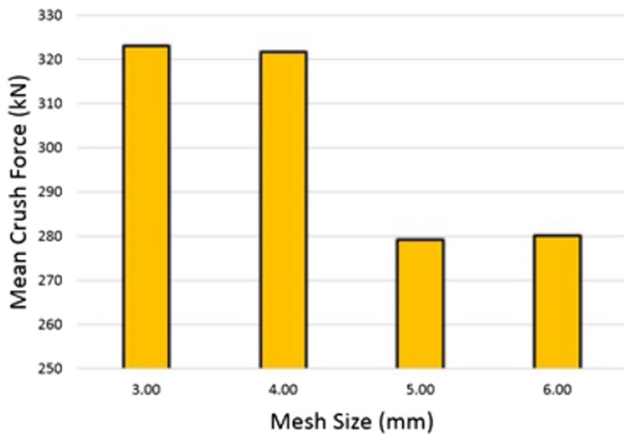


**Fig. 12** Mean crush force comparison for different mesh sizes of bumper beam and crashboxes

## 4 Multi-fidelity optimization concept

High-fidelity models simulate a crash scenario closest to the physical case in a finite element analysis. However, they are computationally expensive models to run especially where many analyses must be done (e.g., for an optimization study). Low-fidelity models decrease the computation time while sacrificing accuracy. To provide a remedy for this problem, multi-fidelity models can be used. Multi-fidelity optimization combines low-fidelity models with few high-fidelity model results to obtain an accurate response prediction while using computationally inexpensive low-fidelity models for optimization runs. In this paper, linear regression multi-fidelity surrogates are used for multi-fidelity optimization as in Zhang et al. [44]. In linear regression multi-fidelity

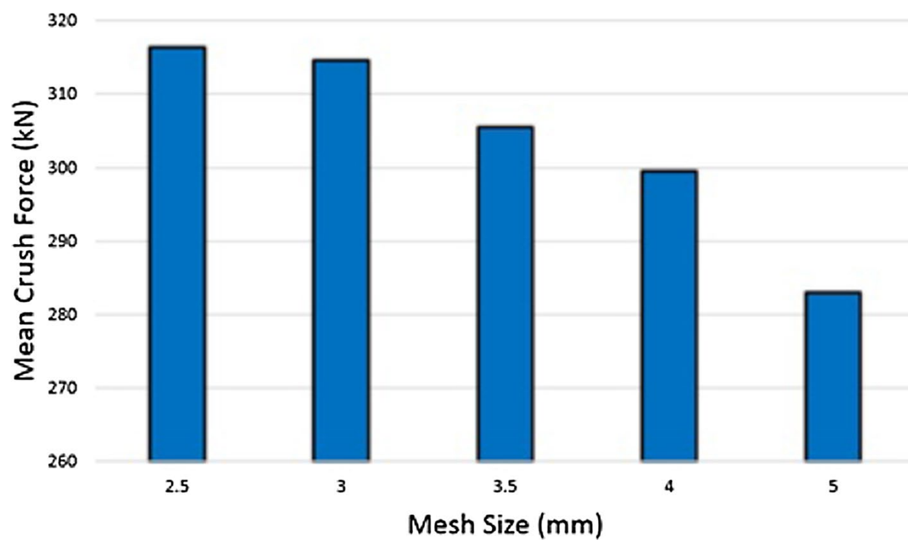


**Fig. 13** Mean crush force comparison for different mesh sizes of honeycomb structures

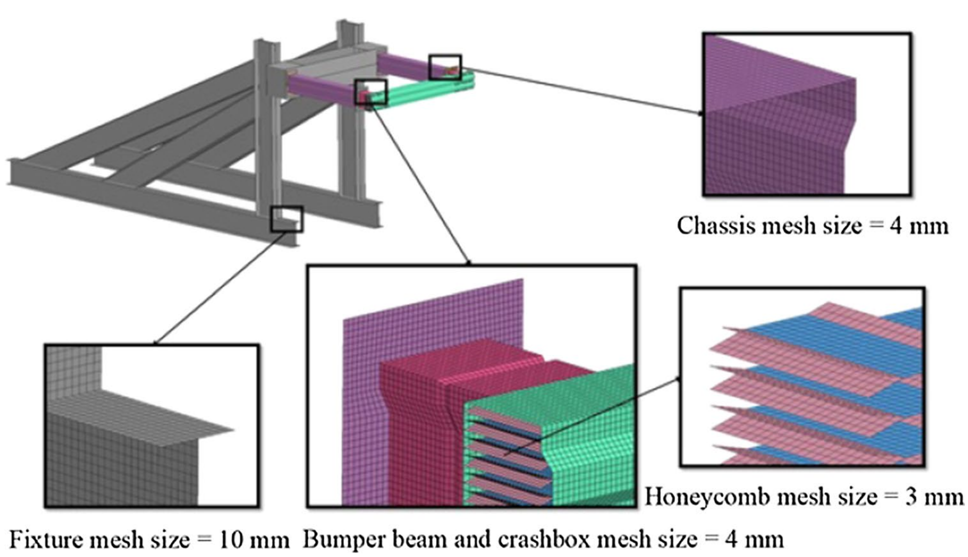


**Fig. 14** Mesh sizes of the high-fidelity finite element model

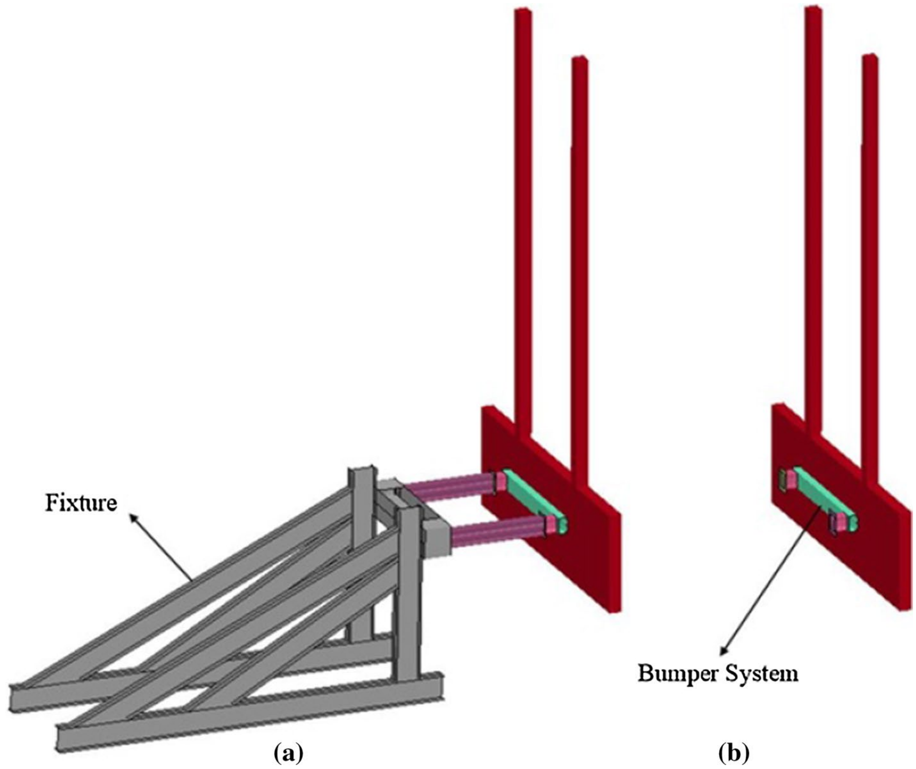


**Fig. 15** **a** High-fidelity model, **b** low-fidelity model

surrogate approach, the low-fidelity finite element response is used as a base function with a scale factor as the regression coefficient. High-fidelity response behavior is expressed as a linear combination of low-fidelity response and a polynomial discrepancy function. Prediction of the response through multi-fidelity surrogate approach is expressed as:

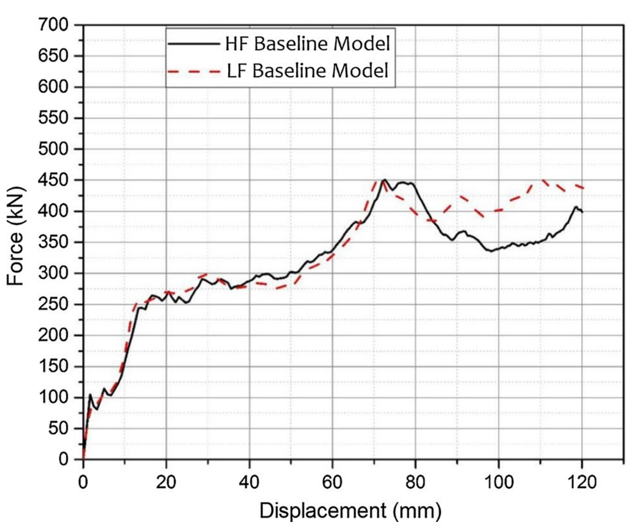


**Fig. 16** Comparison of the low-fidelity (LF) and high-fidelity (HF) models based on the force–displacement behavior for the baseline model

$$\hat{f}_{\mathrm{MF}}(x) = \rho f_L(x) + \delta(x) \tag{7}$$

where $\rho$ is the low-fidelity scale factor, and $\delta(x)$ is the discrepancy function. Because of limited high-fidelity samples, discrepancy function often determined as a constant or a low-order polynomial function. In our study, we used a first-order discrepancy function as

$$\delta(x) = c_0 + \sum_{i=1}^{p} c_i x_i \tag{8}$$

where $x_i$ represents the input variables, $c_i$ is the unknown coefficients of the variables, and $p$ is the number of variables. In order to find the scale factor $\rho$ and coefficients of discrepancy function $\delta(x)$, least square estimation is used. In order to apply least-square method, errors between multi-fidelity surrogates and high-fidelity samples are calculated as

$$e^{(i)} = y_{\mathrm{H}}{}^{(i)} - \hat{f}_{\mathrm{MF}}(x_{\mathrm{H}}{}^{(i)}) \tag{9}$$

where $y_{\mathrm{H}}$ represents the responses of the high-fidelity model computed at the high-fidelity sampling points $x_{\mathrm{H}}$. In vector form, these errors of high-fidelity samples can be written as

$$e = Y - XB \tag{10}$$

where

$$X = \begin{bmatrix} f_L(x_H^{(1)}) & c_1 x_H^{(1)} & \cdots & c_p x_H^{(1)} \\ \vdots & \vdots & \ddots & \vdots \\ f_L(x_H^{(n_H)}) & c_1 x_H^{(n_H)} & \cdots & c_p x_H^{(n_H)} \end{bmatrix},$$
$$Y = \begin{bmatrix} y_H^{(1)} \\ \vdots \\ y_H^{(n_H)} \end{bmatrix}, \quad (11)$$
$$B = \begin{bmatrix} \rho \\ L \\ \theta \\ t \end{bmatrix}$$

where $n_H$ is the number of high-fidelity samples. Finally, the unknown coefficients of discrepancy function and the scale factor are obtained by minimizing the square sum of errors. Unknown coefficients can be expressed as

$$B = (X^T X)^{-1} X^T Y \quad (12)$$

After the calculation of unknown coefficients, multi-fidelity surrogate model for prediction of high-fidelity model response is generated as given in Eq. (7). In the process discrepancy function and scale factor are calculated using common datasets of high- and low-fidelity analyses, while low-fidelity surrogate model is constructed using whole dataset of low-fidelity analyses. The multi-fidelity model is generated using low-fidelity model data and high-fidelity samples in order to predict high-fidelity model response in design space.

## 5 Construction of surrogate models

### 5.1 Design of experiments

Selecting design of experiment (DoE) type is the first step to form a surrogate model. There are two main groups of DoE [13]: classic designs and space filling designs. Full factorial design (FFD), central composite design (CCD) and Box–Behnken design are the most common classic DoE designs. Latin hypercube sampling (LHS) designs, maximum entropy designs, orthogonal arrays, minimax and maximin designs are the most commonly used space filling DoE designs. In this study LHS is used to generate the training points. Detailed explanation of latin hypercube sampling can be found in Acar et al. [13].

Using this DoE technique, 21 training points are generated within the bounds of variables (see Table 2). Generated points are listed in Table 3. Then, FE simulations of both FE models are performed to obtain CFE and SEA responses of FE models at the training points (see Table 4).

**Table 2** Lower and upper bounds of the design variables

| | $L$ (mm) | $\theta$ (deg) | $t$ (mm) |
|---|---|---|---|
| Lower bound | 80 | 30 | 0.25 |
| Upper bound | 160 | 75 | 0.75 |

**Table 3** Design of experiments

| DOE# | $L$ (mm) | $\theta$ (deg) | $t$ (mm) |
|---|---|---|---|
| 1 | 115.8 | 30.00 | 0.5000 |
| 2 | 109.5 | 39.47 | 0.5132 |
| 3 | 130.5 | 65.53 | 0.3026 |
| 4 | 147.4 | 72.63 | 0.4342 |
| 5 | 92.6 | 30.00 | 0.5921 |
| 6 | 105.3 | 63.16 | 0.5395 |
| 7 | 160.0 | 51.32 | 0.2763 |
| 8 | 134.7 | 70.26 | 0.6184 |
| 9 | 126.3 | 53.68 | 0.4605 |
| 10 | 96.8 | 75.00 | 0.3289 |
| 11 | 88.4 | 34.74 | 0.3553 |
| 12 | 101.1 | 48.95 | 0.6711 |
| 13 | 117.9 | 32.37 | 0.6974 |
| 14 | 138.9 | 37.11 | 0.3816 |
| 15 | 113.7 | 41.84 | 0.2500 |
| 16 | 151.6 | 46.58 | 0.4868 |
| 17 | 155.8 | 60.79 | 0.5658 |
| 18 | 84.2 | 58.42 | 0.4079 |
| 19 | 143.2 | 44.21 | 0.7237 |
| 20 | 122.1 | 56.05 | 0.7500 |
| 21 | 80.0 | 67.89 | 0.6447 |

After realization of the FE simulations at the training points, CFE and SEA responses of the high-fidelity model and the low-fidelity model are calculated. These CFE and SEA calculations are tabulated in Table 4. Using corresponding CFE of SEA response of FE models, total of four surrogate models are constructed for HF and LF models.

### 5.2 Accuracy of surrogate models

Response surface models are used to predict actual response of FE model at any point in the design space. Quadratic response surface models are used in this study. Quadratic response surface model can be expressed as [13]

$$\hat{y}(x) = b_0 + \sum_{i=1}^{L} b_i x_i + \sum_{i=1}^{L} b_{ii} x_i^2 + \sum_{i=1}^{L-1} \sum_{j=1}^{L} b_{ij} x_i x_j \quad (13)$$

**Table 4** CFE and SEA responses of finite element models at training points

| DOE# | High fidelity | | | Low fidelity | | |
|---|---|---|---|---|---|---|
| | CFE | SEA (kJ/kg) | *f* | CFE | SEA (kJ/kg) | *f* *f* |
| 1 | 0.7231 | 6.207 | 0.8712 | 0.7288 | 6.865 | 0.8996 |
| 2 | 0.7031 | 6.467 | 0.8756 | 0.6947 | 6.826 | 0.8766 |
| 3 | 0.5937 | 5.909 | 0.7690 | 0.5703 | 5.998 | 0.7440 |
| 4 | 0.6929 | 5.693 | 0.8180 | 0.6844 | 6.112 | 0.8234 |
| 5 | 0.6017 | 5.907 | 0.7739 | 0.6698 | 7.532 | 0.9050 |
| 6 | 0.7707 | 6.781 | 0.9395 | 0.7197 | 6.689 | 0.8826 |
| 7 | 0.5160 | 5.133 | 0.6681 | 0.5429 | 5.579 | 0.6999 |
| 8 | 0.7232 | 5.765 | 0.8421 | 0.7191 | 5.974 | 0.8365 |
| 9 | 0.6904 | 6.355 | 0.8601 | 0.6980 | 6.959 | 0.8862 |
| 10 | 0.6101 | 6.584 | 0.8240 | 0.6495 | 6.404 | 0.8200 |
| 11 | 0.5006 | 6.395 | 0.7416 | 0.5586 | 6.930 | 0.7962 |
| 12 | 0.6869 | 5.757 | 0.8184 | 0.6615 | 6.796 | 0.8527 |
| 13 | 0.7775 | 6.472 | 0.9234 | 0.7533 | 6.416 | 0.8864 |
| 14 | 0.6139 | 5.771 | 0.7727 | 0.6166 | 6.318 | 0.7937 |
| 15 | 0.5268 | 5.771 | 0.7172 | 0.5543 | 6.079 | 0.7391 |
| 16 | 0.6272 | 5.661 | 0.7740 | 0.6683 | 6.255 | 0.8224 |
| 17 | 0.7834 | 5.541 | 0.8657 | 0.7913 | 5.573 | 0.8565 |
| 18 | 0.6573 | 7.464 | 0.9122 | 0.5533 | 7.817 | 0.8496 |
| 19 | 0.7053 | 5.859 | 0.8369 | 0.6775 | 5.934 | 0.8077 |
| 20 | 0.6538 | 6.318 | 0.8343 | 0.6201 | 6.768 | 0.8247 |
| 21 | 0.6665 | 7.575 | 0.9254 | 0.5475 | 7.569 | 0.8301 |

where $\hat{y}(x)$ is the response prediction, $L$ is the size of input vector $\mathbf{x}$ and $b_0$, $b_i$, $b_{ii}$, $b_{ij}$ are the response surface parameters to be determined using linear regression.

In order to construct multi-fidelity surrogate models, all data of LF model and data of HF model at randomly selected 10 training points are used (training points number 1, 4, 5, 6, 7, 10, 11, 13, 14, 18 given in Tables 3 and 4 ). After determination of low-fidelity scale factor ($\rho$) and the discrepancy function ($\delta(x)$), multi-fidelity surrogate model is constructed as it is explained in Sect. 4. Therefore, along with the multi-fidelity surrogates, a total of six surrogate models are constructed in order to predict SEA and CFE responses.

Accuracy of surrogate models is evaluated using the root-mean-square error, RMSE, which can be calculated from:

$$\mathrm{RMSE} = \sqrt{\frac{1}{N}\sum_{k=1}^{N}(y_k - \hat{y}_k)^2} \tag{14}$$

where $y_i$ is the actual response and $\hat{y}_i$ is the surface model response at the $i^{th}$ training point. RMSE value can be normalized with the mean value (see Eq. 15) or the range (see Eq. 16) of the actual responses at the training points as follows:

$$\mathrm{RMSE}_{\mathrm{nor1}} = \frac{\mathrm{RMSE}}{\sum_{k=1}^{N} y_k} \tag{15}$$

$$\mathrm{RMSE}_{\mathrm{nor2}} = \frac{\mathrm{RMSE}}{y_{\max} - y_{\min}} \tag{16}$$

where $y_{\max}$ and $y_{\min}$ are the maximum and minimum values of the responses evaluated at the training points, respectively.

Table 5 provides the RMSE and $\mathrm{RMSE}_{\mathrm{nor}}$ values for the surrogate models constructed for the CFE and SEA prediction. For the surrogate models, it is seen that the $\mathrm{RMSE}_{\mathrm{nor1}}$ values range between 4.9 and 7.6%, $\mathrm{RMSE}_{\mathrm{nor2}}$ values range between 12.7 and 17.6%, and these error values are acceptable for response prediction of a crash as a highly nonlinear phenomenon. It is also noticed that the surrogate models constructed for SEA prediction are more accurate than the ones constructed for CFE prediction.

## 6 Optimization results

The constructed surrogate models are used for optimization of the bumper system to achieve the maximum value of composite objective function ($f$) in Eq. 6. Finite element analyses are performed at these optimum points, and the predicted values of CFE and SEA are compared with the FEA results. The percent error between the predicted values and FEA responses is calculated from

$$\mathrm{Err}_{\mathrm{CFE}} = \frac{|\mathrm{CFE}_{\mathrm{pred}} - \mathrm{CFE}_{\mathrm{fea}}|}{\mathrm{CFE}_{\mathrm{fea}}} \times 100 \tag{17}$$

$$\mathrm{Err}_{\mathrm{SEA}} = \frac{|\mathrm{SEA}_{\mathrm{pred}} - \mathrm{SEA}_{\mathrm{fea}}|}{\mathrm{SEA}_{\mathrm{fea}}} \times 100 \tag{18}$$

### 6.1 High-fidelity optimization results

Using surrogate models for CFE and SEA response prediction of high-fidelity model, optimum values of the design variables are found (Table 6, columns 2, 3 and 4). CFE and SEA responses of the optimum design are predicted using surrogate models (Table 6, columns 5 and 6). Predicted values of composite objective function *f* are calculated using predicted response values (Table 6, column 7). Then, the actual CFE and SEA response values are calculated using finite element simulations (Table 6, columns 8 and 9). Next, the actual value of *f* is calculated using actual response values (Table 6, column 10). Finally, the error in CFE and SEA predictions is calculated using Eqs. (17) and (18) (see Table 6, column 11 and 12).

High-fidelity optimization study yields an optimum design that has actual *f* value of 0.9399. Also CFE and SEA responses of that design are predicted with an error of 2.4% and 3.3%. In order to obtain these results for high-fidelity model, 21 finite element analyses are performed at the training points and a verification run of the optimum point is performed. Therefore, considering that each high-fidelity analysis takes 14 h of computation time, the total cost of high-fidelity optimization is $22 \times 14 = 308$ h of computation time. Note that the computational cost of surrogate model construction and optimization is far smaller than that of a single FE run.

### 6.2 Low-fidelity optimization results

Optimization of low-fidelity model is performed similar to high-fidelity optimization. Optimum values of the design variables (columns 2, 3 and 4), predicted values of CFE, SEA and *f* (columns 5, 6 and 7), finite element response values of CFE, *SEA* and *f* (columns 8, 9 and 10) and errors of CFE and SEA are given in the first row of Table 7 for the low-fidelity model.

Low-fidelity optimization yields on optimum design that has f value of 0.9165, and prediction errors of CFE and SEA are 4.0% and 2.8%, respectively. The composite objective function values of the high-fidelity model and low-fidelity model are very close to each other. Even though these predicted values are very close to each other for different optimum designs, this result is misleading because the actual performance of different designs should be evaluated by using the high-fidelity model.

**Table 5** Accuracy of surrogate models

| | RMSE | $\mathrm{RMSE}_{\mathrm{nor1}}$(%) | $\mathrm{RMSE}_{\mathrm{nor2}}$(%) |
|---|---|---|---|
| Surrogate model for CFE prediction of HF | 0.0499 | 7.6 | 17.6 |
| Surrogate model for SEA prediction of HF | 0.3538 | 5.7 | 14.5 |
| Surrogate model for CFE prediction of LF | 0.0417 | 6.4 | 16.8 |
| Surrogate model for SEA prediction of LF | 0.3214 | 4.9 | 14.3 |
| Surrogate model for CFE prediction of MF | 0.0413 | 6.4 | 14.6 |
| Surrogate model for SEA prediction of MF | 0.3105 | 5.0 | 12.7 |

**Table 6** High-fidelity optimization results

| | *L* mm | *θ* deg | *t* mm | CFE pred. | SEA pred. | *f* pred. | CFE FEA | SEA FEA | *f* FEA | Error CFE | Error SEA |
|---|---|---|---|---|---|---|---|---|---|---|---|
| HF | 80.00 | 75.0 | 0.52 | 0.6867 | 7.679 | 0.9451 | 0.7036 | 7.436 | **0.9399** | 2.4 | 3.3 |

**Table 7** Low-fidelity optimization results

| | *L* mm | *θ* deg | *t* mm | CFE pred. | SEA pred. | *f* pred. | CFE FEA | SEA FEA | *f* FEA | Error CFE | Error SEA |
|---|---|---|---|---|---|---|---|---|---|---|---|
| LF | 105.3 | 30.0 | 0.58 | 0.7170 | 7.015 | 0.9016 | 0.6894 | 7.219 | **0.9165** | 4.0 | 2.8 |
| HF (LF) | 105.3 | 30.0 | 0.58 | 0.7170 | 7.015 | 0.9016 | 0.7573 | 5.516 | **0.8475** | 5.3 | 27.2 |

The second row of Table 7 shows the high-fidelity response values of optimum point obtained from low-fidelity optimization. The actual *f* value of the LF optimum is computed to be 0.8475 (smaller than its LF model predicted value of 0.9165). Also, the errors in CFE and SEA predictions are computed as 5.3% and 27.2%, respectively. Note that the LF and HF models present a good correlation in terms of the force–displacement behavior for the baseline model as shown earlier in Fig. 16. However, for the LF optimum design, the behavior of the low-fidelity and high-fidelity models differed a lot in terms of SEA. As the design space of the optimization problem is wide, this inconsistency is probable.

Computational cost of low-fidelity optimization is much smaller than that of the high-fidelity optimization. In addition to 21 training, one low-fidelity verification is performed. Considering 2.5 h of computation time for LF run $22 \times 2.5 = 55$ h of computational time is spent for LF optimization.

### 6.3 Multi-fidelity optimization results

In the following, the multi-fidelity surrogate model for prediction of high-fidelity response generated using the linear regression multi-fidelity approach is discussed as explained in Sect. 4. Responses of LF model at 21 training points and response of HF model at randomly selected 10 training points (number 1, 4, 5, 6, 7, 10, 11, 13, 14, 18 shown in Table 3 and Table 4) are used. After generation of multi-fidelity model, the same process as high-fidelity optimization is followed. Optimum values of design variables (columns 2, 3 and 4), predicted values of CFE, SEA and f (columns 5, 6 and 7), finite element response values of CFE, SEA and f (columns 8, 9 and 10) and errors of CFE and SEA are given in Table 8 for the multi-fidelity optimum.

The value of composite objective function f is calculated as 0.9238 for high-fidelity FE response of multi-fidelity optimum design. CFE and SEA responses of that design are predicted with an error of 4.5% and 3.1%, respectively. Crash behavior of multi-fidelity optimum bumper design is shown in Fig. 17. Input data to generate multi-fidelity surrogate model required 21 LF model and 10 HF model analyses. In addition, verification of optimum design required an additional HF analysis. Therefore, $21 \times 2.5 + 11 \times 14 = 206.5$ h of computation time is spent.

### 6.4 Comparison of optimization results

Comparing the optimum designs obtained from all FE models, it is seen that the optimum design obtained by using different levels of fidelity is quite different. It is seen that the length of crashboxes ($L$) tends to take values close to the lower limit for the HF optimum and takes higher value for the LF optimum. The multi-fidelity optimum value of $L$ is the same as that of the LF model. The wall angle of honeycombs ($\theta$) takes its upper limit value for HF and MF models, and for the LF model, it takes its lower limit. The wall thickness of honeycombs ($t$) takes values close to middle of design range for HF and LF optimum designs, but the value of $t$ is close to upper limit for the MF optimum design.

Comparing the composite objective function values presented in Tables 6, 7 and 8, it is seen that optimization with HF model provides the optimum design with better performance and smaller error compared to the optimum design obtained through multi-fidelity and low-fidelity models. The composite objective function value of the optimum design obtained through HF model ($f$=0.9399) is 11% larger than that of the optimum design obtained through LF model ($f$=0.8475), and only 2% larger than that of the optimum design obtained through MF model ($f$=0.9238).

Force–displacement responses of all three optimum points obtained through high-fidelity FEA model are shown in Fig. 18. It is seen that the force value of HF optimum design is higher than the LF optimum design at any displacement. Therefore, difference between total energy absorption of HF optimum design and LF optimum design is easily observable at the graph. The behavior of the MF optimum design is different compared to the other two. Average force value of MF optimum design calculated from numerical data lies between the LF and HF optimum designs.

Finally, we provide a comparison in terms of computational cost. To complete 21 finite element simulations for training points and the verification run, 308 h of computation time is spent for high-fidelity optimization. Similarly, 22 low-fidelity FE simulations are completed in 55 h for the optimization with LF model. Finally, for 21 LF model analyses and 11 HF model analyses including the verification run required for multi-fidelity optimization, 206.5 h of computation time is spent.

**Table 8** Multi-fidelity optimization results

| | $L$ mm | $\theta$ deg | $t$ mm | CFE pred. | SEA pred. | $f$ pred. | CFE FEA | SEA FEA | $f$ FEA | Error CFE | Error SEA |
|---|---|---|---|---|---|---|---|---|---|---|---|
| MF | 105.3 | 75.0 | 0.72 | 0.7846 | 6.945 | 0.9592 | 0.7507 | 6.738 | **0.9238** | 4.5 | 3.1 |

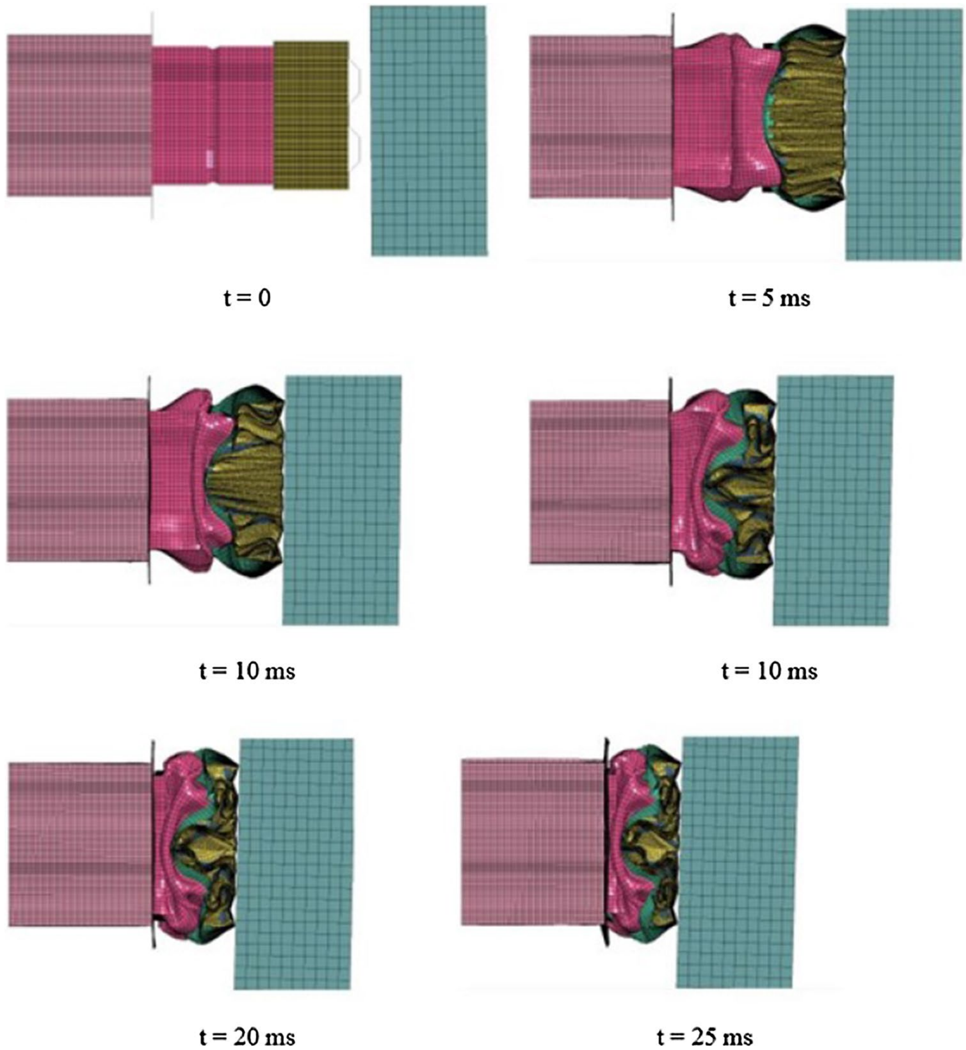


**Fig. 17** Crash behavior of the multi-fidelity optimum bumper system

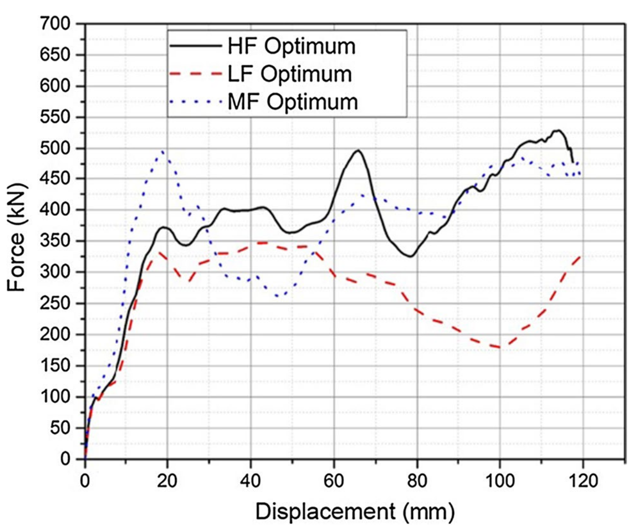


**Fig. 18** Force–displacement responses of the high-fidelity model at optimum points

## 7 Concluding remarks

In this study, surrogate-based multi-fidelity design optimization of a honeycomb filled bumper system was performed to achieve maximum crash force efficiency and specific energy absorption. Two different fidelity finite element models (HF and LF) were considered. The length of the crashboxes, the wall angle of honeycomb structures and the wall thickness of honeycomb structures were taken as design variables. From the results obtained in this study, the following conclusions were drawn:

– Accuracy of response surfaces was evaluated using *RMSE*, normalized with the mean ($RMSE_{\mathrm{nor1}}$) and also with the range ($RMSE_{\mathrm{nor2}}$) of the responses evaluated at the training points. It was seen that $RMSE_{\mathrm{nor1}}$ changed between 4.9 and 7.6%, $RMSE_{\mathrm{nor2}}$ changed between 12.7 and 17.6%, and these error values were found to be acceptable for crash (a nonlinear phenomenon).

– It was also noticed that the surrogate models constructed for SEA prediction are more accurate than the ones constructed for CFE prediction.
– The optimum designs obtained by using different models were quite different. Length ($L$) of MF optimum model was the same as for the LF model, and cell wall angle ($\theta$) value was the same as for the HF model. Honeycomb wall thickness ($t$) values of the HF and LF optimum designs were close to each other, whereas it was close to the upper limit for MF optimum design.
– Optimization with HF model provided the optimum design with better performance and smaller error compared to the optimum design obtained with low-fidelity and multi-fidelity optimizations. The composite objective function value of the optimum design obtained through HF model was 2% larger than that of the optimum design obtained through multi-fidelity optimization and 11% larger than that of the optimum design obtained through LF model.
– Computational time spent to complete high-fidelity optimization was 308 h, whereas it was 206.5 h for multi-fidelity optimization (33% reduction) and 55 h for LF optimization (82% reduction). Multi-fidelity optimization provides a close result to high-fidelity optimization with 33% saving from computation cost.

Lastly, some limitations of the current study can be listed as follows:

– In this study, the HF samples were selected from the pool of LF samples in a random manner. It should be noted that with different set of HF samples the results would be different, and finding a judicious selection procedure of the HF samples is subject of a future study.
– In this study, the peak force values were not penalized in optimization. It should be noted that a high peak force relates to high accelerations, which should be avoided in a crashworthy design. This exercise is subject of a future study.

**Acknowledgements** The support for experimental results provided by the Technology Center at the TOBB University of Economics and Technology, Ankara, Turkey, is gratefully acknowledged.

## Compliance with ethical standards

**Conflict of interest** The authors declare that they have no conflict of interest.

## References

1. Baykasoglu A, Baykasoglu C (2016) Crashworthiness optimization of circular tubes with functionally-graded thickness. Eng Comput 33(5):1560
2. Rouzegar J, Assaee H, Elahi SM, Asiaei H (2018) Axial crushing of perforated metal and composite-metal tubes. J Braz Soc Mech Sci Eng 40(7):349
3. Mou H, Xie J, Su X, Feng Z (2019) Crashworthiness experiment and simulation analysis of composite thin-walled circular tubes under axial crushing. Mech Compos Mater 55(1):121
4. Langseth M, Hopperstad O (1996) Static and dynamic axial crushing of square thin-walled aluminium extrusions. Int J Impact Eng 18(7–8):949
5. Mamalis A, Manolakos D, Spentzas K, Ioannidis M, Koutroubakis S, Kostazos P (2009) The effect of the implementation of circular holes as crush initiators to the crushing characteristics of mild steel square tubes: experimental and numerical simulation. Int J Crashworthiness 14(5):489
6. Lu R, Liu X, Zhang S, Chen S, Hu X, Liu L (2018) Experiment and simulation to compress destroyed process of novel tailor rolled tubes. J Braz Soc Mech Sci Eng 40(9):445
7. Najafi A, Rais-Rohani M (2008) Influence of cross-sectional geometry on crush characteristics of multi-cell prismatic columns. In: 49th AIAA/ASME/ASCE/AHS/ASC structures, structural dynamics, and materials conference, 16th AIAA/ASME/AHS adaptive structures conference, 10th AIAA non-deterministic approaches conference, 9th AIAA Gossamer spacecraft forum, 4th AIAA multidisciplinary design optimization specialists conference , p. 2014
8. Djamaluddin F, Abdullah S, Ariffin A, Nopiah Z (2015) Non-linear finite element analysis of bitubal circular tubes for progressive and bending collapses Non-linear finite element analysis of bitubal circular tubes for progressive and bending collapses. Int J Mech Sci 99:228
9. Fang J, Gao Y, Sun G, Zheng G, Li Q (2015) Dynamic crashing behavior of new extrudable multi-cell tubes with a functionally graded thickness. Int J Mech Sci 103:63
10. Pang T, Zheng G, Fang J, Ruan D, Sun G (2019) Energy absorption mechanism of axially-varying thickness (AVT) multicell thin-walled structures under out-of-plane loading. Eng Struct 196:109130
11. Paygozar B, Sadigh M (2020) Practicability of metallic hybrid systems in enhancing the energy absorption capacity: expansion and buckling mechanisms. J Braz Soc Mech Sci Eng 42
12. Mamalis A, Johnson W (1983) The quasi-static crumpling of thin-walled circular cylinders and frusta under axial compression. Int J Mech Sci 25(9–10):713
13. Acar E, Guler M, Gerceker B, Cerit M, Bayram B (2011) Multi-objective crashworthiness optimization of tapered thin-walled tubes with axisymmetric indentations. Thin-Walled Struct 49(1):94
14. Yin H, Wen G, Fang H, Qing Q, Kong X, Xiao J, Liu Z (2014) Multiobjective crashworthiness optimization design of functionally graded foam-filled tapered tube based on dynamic ensemble metamodel. Mater Des 55:747
15. Reid S, Reddy T (1986) Static and dynamic crushing of tapered sheet metal tubes of rectangular cross-section. Int J Mech Sci 28(9):623
16. Nagel GM, Thambiratnam DP (2006) Dynamic simulation and energy absorption of tapered thin-walled tubes under oblique impact loading. Int J Impact Eng 32(10):1595

17. Acar E, Altin M, Güler M (2019) Evaluation of various multi-cell design concepts for crashworthiness design of thin-walled aluminum tubes. Thin-Walled Struct 142:227
18. Santosa S, Wierzbicki T (1998) Crash behavior of box columns filled with aluminum honeycomb or foam. Comput Struct 68(4):343
19. Zarei H, Kröger M (2008) Optimum honeycomb filled crash absorber design. Mater Des 29(1):193
20. Xu S, Beynon JH, Ruan D, Lu G (2012) Experimental study of the out-of-plane dynamic compression of hexagonal honeycombs. Compos Struct 94(8):2326
21. He Q, Ma D, Zhang Z, Yao L (2015) Mean compressive stress constitutive equation and crashworthiness optimization design of three novel honeycombs under axial compression. Int J Mech Sci 99:274
22. Galehdari SA, Kadkhodayan M (2019) Collapse of honeycomb cell as a result of buckling or plastic hinges, analytical, numerical and experimental study. J Braz Soc Mech Sci Eng 41(3):154
23. Li Z, Yu J, Guo L (2012) Deformation and energy absorption of aluminum foam-filled tubes subjected to oblique loading. Int J Mech Sci 54(1):48
24. Altin M, Güler MA, Mert SK (2017) The effect of percent foam fill ratio on the energy absorption capacity of axially compressed thin-walled multi-cell square and circular tubes. Int J Mech Sci 131:368
25. Sarkabiri B, Jahan A, Rezvani MJ (2017) Crashworthiness multi-objective optimization of the thin-walled grooved conical tubes filled with polyurethane foam. J Braz Soc Mech Sci Eng 39(7):2721
26. Altin M, Acar E, Güler M (2018) Foam filling options for crashworthiness optimization of thin-walled multi-tubular circular columns. Thin-Walled Struct 131:309
27. Park DK (2011) A development of simple analysis model on bumper barrier impact and new IIHS bumper impact using the dynamically equivalent beam approach. J Mech Sci Technol 25(12):3107
28. Tanlak N, Sonmez FO, Senaltun M (2015) Shape optimization of bumper beams under high-velocity impact loads. Eng Struct 95:49
29. Belingardi G, Beyene A, Koricho E, Martorana B (2015) Alternative lightweight materials and component manufacturing technologies for vehicle frontal bumper beam. Compos Struct 120:483
30. Liu Z, Lu J, Zhu P (2016) Lightweight design of automotive composite bumper system using modified particle swarm optimizer. Compos Struct 140:630
31. Srinivas GR, Deb A, Chou CC (2016) Lightweighting of an automotive front end structure considering frontal ncap and pedestrian lower leg impact safety requirements. Tech. rep, SAE Technical Paper
32. Patil R, Lande P, Tadamalle A, Reddy Y (2017) Determination of impact absorbing capacity and toughness of aluminum honeycomb sandwich panel in bumper beam. Mater Today Proc 4(8):8816
33. Wang C, Li Y, Zhao W, Zou S, Zhou G, Wang Y (2018) Structure design and multi-objective optimization of a novel crash box based on biomimetic structure. Int J Mech Sci 138:489
34. Karthikeyan M, Jenarthanan M, Giridharan R, Shunmugesh K (2019) Investigation on crash analysis of a frontal car bumper. Trans Indian Inst Met 72(10):2699
35. Li Z, Yu Q, Zhao X, Yu M, Shi P, Yan C (2017) Crashworthiness and lightweight optimization to applied multiple materials and foam-filled front end structure of auto-body. Adv Mech Eng 9(8):1687814017702806
36. Jacob A, Arunkumar O (2016) Improving the crashworthiness of an automobile bumper. In: International conference on emerging trends in engineering and management , pp 67–79
37. Sun G, Li G, Stone M, Li Q (2010) A two-stage multi-fidelity optimization procedure for honeycomb-type cellular materials. Comput Mater Sci 49(3):500
38. Vitali R, Haftka RT, Sankar BV (2002) Multi-fidelity design of stiffened composite panel with a crack. Struct Multidiscip Optim 23(5):347
39. Viana FA, Steffen V, Butkewitsch S, de Freitas LM (2009) Optimization of aircraft structural components by using nature-inspired algorithms and multi-fidelity approximations. J Global Optim 45(3):427
40. Ghoman SS, Kapania RK, Chen P, Sarhaddi D, Lee D (2012) Multifidelity, multistrategy, and multidisciplinary design optimization environment. J Aircraft 49(5):1255
41. Huang E, Xu J, Zhang S, Chen CH (2015) Multi-fidelity model integration for engineering design. Proc Comput Sci 44:336
42. Park C, Haftka RT, Kim NH (2017) Remarks on multi-fidelity surrogates. Struct Multidiscip Optim 55(3):1029
43. Chaudhuri A, Lam R, Willcox K (2018) Multifidelity uncertainty propagation via adaptive surrogates in coupled multidisciplinary systems. AIAA J pp 235–249
44. Zhang Y, Kim NH, Park C, Haftka RT (2018) Multifidelity surrogate based on single linear regression. AIAA J 56(12):4944
45. Redhe M, Nilsson L (2006) A multipoint version of space mapping optimization applied to vehicle crashworthiness design. Struct Multidiscip Optim 31(2):134
46. Larsen AA, Bendsøe M, Hattel J, Schmidt H (2009) Optimization of friction stir welding using space mapping and manifold mapping an initial study of thermal aspects. Struct Multidiscip Optim 38(3):289
47. Florentie L, Blom DS, Scholcz TP, van Zuijlen AH, Bijl H (2016) Analysis of space mapping algorithms for application to partitioned fluid-structure interaction problems. Int J Numer Meth Eng 105(2):138
48. Siegler J, Ren J, Leifsson L, Koziel S, Bekasiewicz A (2016) Supersonic airfoil shape optimization by variable-fidelity models and manifold mapping. Proc Comput Sci 80:1103
49. Jansson T, Andersson A, Nilsson L (2005) Optimization of draw-in for an automotive sheet metal part: an evaluation using surrogate models and response surfaces. J Mater Process Technol 159(3):426
50. Jiang P, Xie T, Zhou Q, Shao X, Hu J, Cao L (2018) A space mapping method based on Gaussian process model for variable fidelity metamodeling. Simul Model Pract Theory 81:64
51. Hallquist JO et al (2006) LS-DYNA theory manual. Livermore Software Technology Corporation 3:25
52. E.R. No. 29: Uniform provisions concerning the approval of vehicles with regard to the protection of the occupants of the cab of a commercial vehicle (2012)
53. Mayrhofer E, Steffan H, Hoschopf H (2005) Enhanced coach and bus occupant safety. Enhanced coach and bus occupant safety (na)
54. Goldberg DE (1989) Genetic algorithms in search, optimization and machine learning. Addison-Wesley Longman Publishing Co., Inc.
55. Zhang X, Zhang H, Wen Z (2014) Experimental and numerical studies on the crush resistance of aluminum honeycombs with various cell configurations. Int J Impact Eng 66:48
56. Güler MA, Cerit ME, Mert SK, Acar E (2020) Experimental and numerical study on the crashworthiness evaluation of an intercity coach under frontal impact conditions. Proc Inst Mech Eng D J Automob Eng. https://doi.org/10.1177/0954407020927644